AVEIRO - PORTUGAL

Please cite this article as: Debasu, Mengistie L.; Riedl, Jesse C.; Rocha, João, Carlos, Luís. D. *Li^{+} Role in Upconversion Emission Enhancement of $(YYbEr)_2O_3$ Nanoparticles* **Nanoscale**, 2018,10, 15799-15808

Received 00th January 20xx,
Accepted 00th January 20xx

DOI: 10.1039/x0xx00000x

www.rsc.org/

Li^+ Role in Upconversion Emission Enhancement of $(YYbEr)_2O_3$ Nanoparticles

Mengistie L. Debasu,[a,b]* Jesse C. Riedl,[b] J. Rocha,[b] and Luís D. Carlos[a]*

The mechanism of upconversion enhancement for Li^+-doped materials is still contentious. Attempting to settle the debate, here upconversion emission enhancement of $(Y_{0.97-x}Yb_{0.02}Er_{0.01}Li_x)_2O_3$, x=0.000–0.123, nanoparticles is studied. Li^+ incorporation in the Y_2O_3 host lattice is achieved via co-precipitation and solid-state reaction routes. In contrast with numerous reports, elemental analysis reveals the former method does not afford Li^+-bearing nanoparticles. The solid-state reaction route accomplishes an effective Li^+ doping, as witnessed by inductively coupled plasma atomic emission spectroscopy and X-ray photoelectron spectroscopy (XPS). Transmission electron microscopy and powder X-ray diffraction yield nanoparticle sizes increasing with increasing Li^+ concentration. Rietveld refinement of powder X-ray diffraction data shows the cubic lattice parameter decreases with increasing Li^+ content. Emission quantum yield increases tenfold with increasing Li^+ content up to x=0.123, reaching a maximal value of 0.04% at x=0.031. XPS and infrared spectroscopy show the carbonate groups increase with increasing Li^+ content, thus not supporting the prevailing view that the upconversion luminescence enhancement observed upon Li^+ nanoparticle's doping is due to the decrease of the number of quenching carbonate groups present. Rather, particle size increment and the decrease in the lattice parameter of the host crystals are shown to be the prime sources of quantum yield enhancement.

Introduction

Photon upconversion is a nonlinear optical process converting low-energy (e.g., infrared) excitation photons into high-energy (visible) emission photons, with a strong dependence on the excitation power. Over the past few years, upconversion has received much attention in the fields of nanotechnology, nanomedicine and photovoltaics.[1–4] In particular, trivalent lanthanide ions (Ln^{3+}) are ideal for photon upconversion because of their ladder-like intra-4f electronic structures, and unique luminescence features, such as large anti-Stokes emissions, sharp emission bands, and long excited-state lifetimes. For instance, Er^{3+} and Tm^{3+} have been widely used for light emission in the ultraviolet to near-infrared spectral region via Yb^{3+} sensitization upon 980 nm excitation.[5–8] However, due to the parity forbidden character of the intra-4f transitions and the nonlinear processes in photon upconversion, the Ln^{3+} emission intensity is in general too low to fulfil the growing demand for developing efficient light emitting materials. In this context, increasing the Ln^{3+} light absorption and upconversion emission efficiency (given by the absolute emission quantum yield) have been the primary focus of researchers working on various technological applications.[9–13] Moreover, the determination of the absolute emission quantum yields of upconverting nanoparticles have been scarcely reported and hindered by both technical and experimental challenges.[14–21]

Ln^{3+} emission intensity depends on factors, such as the type and size of the host material, and the relative Ln^{3+} concentration in the host crystal. For instance, fluorides are among the most efficient host materials for Ln^{3+} upconversion, due to their lowest cut-off phonon energy (ca. 350 cm^{-1}). Yet, compared to the oxide hosts with typical phonon energy in excess of 600 cm^{-1}, fluoride-based upconversion systems have poor chemical and thermal stability,[5,22,23] often precluding their practical application. Hence, certain physical and chemical properties of the host material and their impact on the Ln^{3+} luminescence features are crucial to achieve the target applications.

Various strategies have been employed to enhance the upconversion emission of host-embedded Ln^{3+} ions,[24–28] including surface coating and core-shell structuring, changing the Ln^{3+} concentration, and co-doping with alkaline ions.[29–34] A significant progress has been made concerning the former two strategies, and the photon upconversion processes and enhancement mechanisms are well surveyed. In contrast, despite some promising results, the Ln^{3+} emission enhancement induced by alkaline ions doping is contentious and poorly understood. Table S1 in ESI reviews Li^+-doped host materials (fluorides, oxides, phosphates, vanadates and glasses) used to study Ln^{3+} upconversion enhancement. The proposed enhancement mechanisms encompass distortion of the activator ions local crystal field symmetry,[35–39] charge compensation,[40,41] reduction of the number of quenching centres,[42,43] improved crystallinity,[44,45] and particle/crystallite size increase.[42,46] Li^+ is assumed to easily enter and diffuse in the host lattice occupying, due to its small radius, both the interstitial and substitutional sites, changing the local crystal field symmetry, and relaxing the parity forbidden character of the intra-4f transitions. Therefore, the distortion of the local field symmetry at emitting Ln^{3+} has been the most common explanation for Li^+-induced emission enhancement (Table S1 in ESI). On the other hand, Li^+ doping may improve crystallinity and increase the particle or crystallite size, due to the lower melting temperature of Li precursors.[33,42,46–51] Doping with Li^+ ions may also decrease the number of quenching centres, such as OH^- and CO_2^{3-}, on the surface of the nanoparticles, increasing upconversion emission by reducing non-radiative transitions.[42,46,49,52–61] In addition, Li^+ may act as a charge compensating ion when Ln^{3+} replace non-trivalent cations.[41,62] Another explanation for the upconversion emission

[a] *Department of Physics and CICECO – Aveiro Institute of Materials, University of Aveiro, 3810-193 Aveiro, Portugal.*
[b] *Department of Chemistry and CICECO – Aveiro Institute of Materials, University of Aveiro, 3810-193 Aveiro, Portugal.*
* Corresponding author: debasu@ua.pt; lcarlos@ua.pt.
Electronic Supplementary Information (ESI) available: Review Table S1, Quantum Yield Measurement Setup, Crystallite Size and Rietveld Refinement, Electron Microscopy, Infrared Spectroscopy, Thermogravimetry, and Radiant and Luminous Fluxes (Table S2). See DOI: 10.1039/x0xx00000x

enhancement is an increased lifetime of the intermediate excited states of the activator ions (Table S1 in ESI).[61,63–71]

The aforementioned mechanisms for Li^+-enhanced upconversion in various hosts, including Y_2O_3 nanocrystals, are essentially speculative. Surprisingly, the studies often disregard both Li^+ elemental analysis, and careful luminescence quantum yield measurements (see Table S1 in ESI).[30,31,36,37,42,43,49,52,53,59–62,67,69,72–79] For instance, we found that a co-precipitation synthesis procedure,[31] comprising washing and centrifugation steps results in Li^+ free Y_2O_2 nanoparticles. In fact, the presumed Li^+-doped upconversion materials obtained *via* solution synthesis methods have not been assessed by elemental analysis and may not contain any lithium, exception for a few studies.[9,32,45,80] Furthermore, the reported enhancement and emission efficiency have usually been based solely on the relative emission intensity (arbitrary units), Table S1 in ESI. This has led to erroneous conclusions because the emission intensity strongly depends on many experimental factors, including the measurement conditions (e.g., absorption cross-section, sample volume, sample preparation and optical setup), even for the same sample measured at a different time.

Here, we wish to report the first quantitative assessment of Li^+-induced upconversion enhancement based on the measurement of absolute emission quantum yields and using $(Y_{0.97-x}Yb_{0.02}Er_{0.01}Li_x)_2O_3$ nanocrystals, x=0.000–0.123, as a model system. Co-precipitation and solid-state reaction synthesis methods are appraised for their ability to effectively dope nanocrystals with Li^+. Inductively coupled plasma atomic emission spectroscopy (ICP-AES) revealed that the co-precipitation synthesis procedure yields no Li^+ in the final upconversion nanocrystals. We stress, this conclusion is valid only for the synthesis of lanthanide oxides. The unit cell parameter of the host lattice and crystallite size determined the upconversion enhancement.

Experimental Details

Materials: Y_2O_3 (99.9%), Yb_2O_3 (99.9%) and Er_2O_3 (99.9%) (Jinan Henghua Sci. & Tec. Co., Ltd.) were purchased and dissolved separately in ultra-pure nitric acid (HNO_3 65%, PA-ISO) to obtain the respective lanthanide nitrate solutions, i.e., $Y(NO_3)_3$, $Yb(NO_3)_3$ and $Er(NO_3)_3$. $LiNO_3{\cdot}xH_2O$ (Sigma-Aldrich, ≥98.0%) was used as a Li^+ precursor. Urea (Sigma-Aldrich, ≥98.0%), Hexadecyltrimethylammonium bromide (CTAB) (Sigma-Aldrich, ≥98.0%) and citric acid monohydrate (Sigma-Aldrich, ≥98.0%) were also used in the synthesis. Chemicals were used as received without further purification. In all experiments, distilled water and absolute ethanol (Fisher Scientific, 99.5%) were used.

Synthesis Methods: i) Co-precipitation Method. A modified co-precipitation procedure reported by Gai et al.,[81] was used to prepare Li^+ doped $(Y_{0.97}Yb_{0.02}Er_{0.01})_2O_3$ spherical nanoparticles. Briefly, aqueous solutions of $Y(NO_3)_3$ (2.760 mL, 0.4 M), $Yb(NO_3)_3$ (0.060 mL, 0.4 M), $Er(NO_3)_3$ (0.120 mL, 0.1 M) and $LiNO_3$ (0.300 mL, 0.2 M)) were mixed in a round-bottom-flask. Distilled water (265 mL), urea (2.7 g) and CTAB (0.6 g) were added to this mixture. After 30 minutes of vigorous stirring and 3 minutes of ultra-sonication, the solution was heated up at 85 °C for 2 hours. After cooling to room temperature, the precursor was separated by centrifugation, and washed several times with deionized water and finally with ethanol. The precursor was dried at 75 °C in air for at least 12 hours. To obtain crystalline $(Y_{0.92}Yb_{0.02}Er_{0.01}Li_{0.05})_2O_3$ nanoparticles, the precursor was calcined at 800 °C for 3 hours with heating and cooling rates of 2 and 5 °C/minute. $(Y_{0.97-n}Yb_{0.02}Er_{0.01}Li_n)_2O_3$ nanoparticles with nominal n=0.15 were prepared following the same procedure by changing the relative concentration of Li^+ and Y^{3+}.

ii) Sol–Gel Mixing and Solid-State Reaction Method. Li^+ doped $(Y_{0.97}Yb_{0.02}Er_{0.01})_2O_3$ nanoparticles were synthesized *via* a solid-state reaction following a modified procedure.[45,82] In a typical synthesis, aqueous solutions containing $Y(NO_3)_3$ (7.680 mL, 0.4 M), $Yb(NO_3)_3$ (0.160 mL, 0.4 M), $Er(NO_3)_3$ (0.320 mL, 0.1 M) and $LiNO_3$ (0.160 mL, 0.2 M)) were mixed in a 10 ml glass vial under magnetic stirring and ultra-sonication for 15 minutes. The solution was dried at 75 °C in air for at least 24 hours until the water completely evaporated. Subsequently, citric acid (with citric acid to Y, Yb, Er and Li molar ratio of 2.5:1.0) was dissolved thoroughly in absolute ethanol (10 mL) and the mixture was stirred vigorously until it became a transparent solution. The ethanol-citric acid solution was poured into the dried salt and stirred and sonicated for additional 30 minutes. The solution was heated up at 80 °C to vaporize excessive solvent until it became highly viscous and changed into a transparent glassy gel. No visible precipitation was observed during gelation. The transparent xerogel was ground into fine white powder and calcined at 800 °C for 1 hour with heating and cooling rates of 5 °C/minute. This procedure yields upconverting $(Y_{0.96}Yb_{0.02}Er_{0.01}Li_{0.01})_2O_3$ nanoparticles. The same procedure was used to prepare $(Y_{0.97-n}Yb_{0.02}Er_{0.01}Li_n)_2O_3$ nanoparticles with nominal n=0.000, 0.025, 0.050, 0.100 and 0.150 by changing only the relative concentration of Li^+ and Y^{3+}.

X-Ray Diffraction (XRD): powder XRD patterns were recorded in the range $15°\leq 2\theta \leq 95°$ on a PANalytical Empyrean X-ray diffractometer operating at 45 kV and 40 mA ($Cu_{K\alpha 1}$ radiation source at 1.5406 Å) in reflection spinning scan mode with a 0.013° step size. Nanocrystal's sizes were calculated using Scherrer's equation. Rietveld refinement of the measured diffraction patterns was performed using HighScore Plus software suit and the reference data of cubic Y_2O_3 (04-007-9751) taken from the International Centre for Diffraction Data database.

Electron Microscopy: The morphology of the nanoparticles was examined on a Hitachi H9000-NA transmission electron microscopy (TEM) with an acceleration voltage of 300 kV and a Hitachi HD-2700 scanning transmission electron microscopy (STEM) operating at an acceleration voltage of 200 kV.

Inductively Coupled Plasma Atomic Emission Spectroscopy (ICP-AES): *Elemental analysis of* the samples was performed with an ICP-AES (Jobin Yvon Activa M).

Fourier Transform Infrared Spectroscopy (FTIR): spectra were recorded on a Bruker FTIR TENSOR 27. For the reflectance mode, the powders were measured without further preparation, while for the transmission mode pallets were pressed. Each powdered sample (1.5 mg) was mixed with 200 mg KBr. The mixture was ground and pressed uniaxial with 9 tons for 2 minutes, and semi-transparent pallets were obtained. Spectra were recorded between 350 and 4000 cm^{-1} with 256 scans and 4 cm^{-1} resolution.

Thermogravimetric Analysis (TGA): Between 7 and 15 mg samples were analysed on a thermogravimetric analyser TGA-50 from

Shimadzu. The samples were heated from room temperature to 800 °C with a rate of 5 °C/minute and the weight loss was measured every second.

X-Ray Photoelectron Spectroscopy (XPS): XPS spectra were acquired in an ultra-high vacuum system with a base pressure of 2×10^{-10} mbar. The system is equipped with a hemispherical electron energy analyser (SPECS Phoibos 150), a delay-line detector and a monochromatic $Al_{K\alpha}$ (1486.74 eV) X-ray source. High resolution spectra were recorded at normal emission take-off angle and with a pass-energy of 20 eV, which provides an overall instrumental peak broadening of 0.5 eV. The powder samples were suspended in milli-Q water and drop coated on Si wafers. The samples were measured using an electron gun for charge compensation. The binding energy spectra peak positions were corrected by the difference between the measured C1s binding energy peak positions for each sample and the reference at 284.8 eV, proposed by Boyd *et al.*[83]

Radiant Flux and Upconversion Quantum Yield Measurements: The emission spectral radiant flux of powder samples was measured using an integrating sphere (ISP 150L-131, Instrument Systems) as was previously reported,[16,84] Figure S1 in ESI. All the spectra were acquired with a resolution of 0.1 nm, 20 s integration time and 2 averaged spectra scans in the wavelength range of 500 to 720 nm. The integrating sphere ($BaSO_4$ coating) has an internal diameter of 150 mm and was coupled to an array spectrometer (MAS-40, Instrument Systems). The measurements have an accuracy of 10%, according to the manufacturer. The excitation source was a NIR continuous wave laser diode (MDL-H-980, PSU-H–LED power source controller, CNI Lasers, maximum output power 5 W), emitting a nearly Gaussian beam centred at 980 nm (TEM_{00} mode, accordingly to the manufacturer). The laser beam was coupled into a customized optical fibre (SarSpec, 0.6 mm core diameter with an adaptable-length ferrule) that guides the excitation beam to the sample compartment consisting of a quartz tube (outer diameter of 5.0 mm) placed at the entrance of the integrating sphere port (Figure S1 in ESI). The quartz tube was loaded with 20 mg of nanoparticle powder for each sample. The incident laser power (in units of W) on sample's illuminated area was measured with a Thermopile-S310C (Thorlabs) power meter. The laser power density was computed using the ratio between the excitation power and the illuminated area (in cm^{-2}). The illuminated area is calculated using the numerical aperture of the fibre (0.22) and the characteristic geometrical arrangement of the setup (distances, angles, quartz wall thickness). The radiant spectral flux of the samples was measured for laser power densities up to 640 W cm^{-2}. The background spectral flux was subtracted taking into account the contribution of the reflection coming from the sample holder by recording the respective spectra of an empty sample holder.

Results and Discussion

Table 1 shows ICP-AES elemental analysis of spherical $(Y_{0.97-n}Yb_{0.02}Er_{0.01}Li_n)_2O_3$ nanoparticles with nominal n=0.05 and 0.15, prepared by the co-precipitation method. While the nominal Er^{3+} and Yb^{3+} concentration of both samples is close to the measured concentration, no Li^+ was detected indicating its removal by the centrifugation and washing steps. In conclusion, the co-precipitation method does not afford Li^+ doped nanoparticles and, thus, the issuing materials were not further studied. Importantly, the Li^+-induced luminescence enhancement studies previously reported for materials obtained by similar co-precipitation method (Table S1 in ESI) should be reassessed, taking into consideration proper lithium elemental analysis.

In contrast, materials prepared by the solid-state reaction method contain lithium in concentrations in fair agreement with the nominal ones (Table 2). Thus, these samples were further studied.

The powder XRD patterns of the nanoparticles with x=0.000, 0.008, 0.018, 0.031, 0.070 and 0.123 are indexed as cubic Y_2O_3 (reference to card 04-007-9751), Figure 1A. No additional peaks are observed and, thus, no other crystalline phases are present. Scherrer's equation indicates the crystallite size increases with increasing Li^+ concentration (Figure 1B). Accordingly, crystallite sizes of 20.3±0.6, 30.2±1.0, 56.6±4.4, 74.9±6.0, 72.5±5.7 and 81.3±7.2 nm were obtained for the nanoparticles with x=0.000, 0.008, 0.018, 0.031, 0.070 and 0.123, respectively. Rietveld-refinement show the lattice parameter decreases with increasing Li^+ concentration (Figure 1C and Figure S2-S3 in ESI), indicating the incorporation of Li^+ in the host lattice. ICP-AES elemental analysis results clearly show charge compensation is attained, according to the formula $(Y_{0.97-x}Yb_{0.02}Er_{0.01}Li_x)_2O_3$. However, Li^+ is not expected to replace Y^{3+} but rather, due to its small size and lower electronegativity, Li^+ most likely occupies the interstitial sites within the first Y^{3+} coordination sphere, attracting O^{2-} ions, and resulting in the observed lattice constant shrinkage. A similar level of lattice parameter shrinkage was noted for Gd_2O_3,[30] Y_2O_3,[36,42] $NaGdF_4$[34] and $GdVO_4$[50] hosts upon Li doping.

Representative TEM images and particle size distributions are shown in Figure 2 and Figure S4. As expected, the nanoparticles are somewhat clustered, a limitation of the solid-state synthesis route, and have an irregular habit not far from spherical. The particle size increases with Li^+ content (Figure 2 and Figure S4), 21±6, 31±11, 88±25, 86±26, 80±26 and 102±24 nm, for x=0.000, 0.008, 0.018, 0.031, 0.070, and 0.123, respectively. The nanoparticles size obtained by XRD and TEM are in good agreement, Figure 1B.

Similar results have been reported for other upconversion host materials, including Y_2O_3,[42,49,69] Lu_2O_3,[46] Y_2SiO_3,[49,77,80] $GdVO_4$,[85] and $Lu_6O_5F_8$.[86] The observed increase in crystallite and particle sizes are attributed to the flux effect of Li^+ ions during the reaction as the precursor $LiNO_3$ melts above 255 °C.[86] Chen *et al.*,[87] investigated the flux effect of Li_2CO_3 and reasoned that the lower Li_2CO_3 melting temperature leads to the formation of highly crystalline particles with larger crystallite sizes through the flux effect as the Li_2CO_3 melts and generates a liquid phase. The liquid phase promotes the diffusion of ions, and accelerates the crystallization process.[88] Moreover, crystallite growth is stimulated by the formation of a liquid phase between the grain boundaries, which decreases energy loss on the surface.[89] This effect is the likely reason for the particle agglomeration, and

particle or crystallite size increment upon increasing the $LiNO_3$ content.

FTIR spectra exhibit absorption bands at 1500 cm^{-1} and 860 cm^{-1} attributed to carbonate groups CO_3^{2-}, due to adsorption of CO_2 on the surface of the nanoparticles, whose intensity increases with increasing Li^+ content (Figure S5).[69,75,76,90] The presence of OH^- species on the surface of the nanocrystals is witnessed by bands at 3350 cm^{-1}. It is often considered (Table S1 in ESI) that Li^+ ions decrease the number of quenching centres, such as OH^-, CO_3^{2-}, on the surface of the nanoparticles, suggesting that Li^+ enhanced upconversion emission can be achieved by decreasing non-radiative transition channels.[42,46,61,49,52,53,55,57–60] FTIR, however, is neither a surface technique nor a priori quantitative, and conclusions on the number of surface groups and quenching centres should be regarded with caution. Indeed, we have observed that CO_3^{2-} bands increase monotonously (rather than decrease) with Li^+ doping (Figure S5).

Thermogravimetry shows the overall weight loss between room temperature and 800 °C is less than 1.6% for all samples: 1.57, 0.67, 0.59, 1.22, 1.56 and 1.18%, for *x*=0.000, 0.008, 0.018, 0.031, 0.070 and 0.123, respectively (Figure S6). The values are too small and the differences are not significant to draw safe conclusions on the variation in the number of hydroxyl and carbonate groups present.[91]

Figure 3 shows XPS spectra in the C1s, O1s, Y3d, Yb4d/Er4d and Er5s/Li1s/Yb5s regions for the nanoparticles with *x*=0.000 and 0.070. The carbon C1s peaks, ascribed to adventitious carbon,[83,92,93] at 284.8 eV and 289.7 eV are given by C-C and O-C=O bonds,[94] respectively (Figure 3A). The relatively strong O-C=O bond observed for the higher Li^+ content sample indicates that more carbon-bearing groups are present on the surface of these nanoparticles. This is consistent with the FTIR evidence (Figure S5). O1s peaks at 529.2 and 531.3 eV, respectively, are attributed to the oxygen bonding in the Y_2O_3 lattice[95,96] and in the OH groups on the surface of the nanoparticles,[97,98] Figure 3B. Taking the relative intensities of these two O1s peaks into account, no significant change in the number of OH groups is observed. The $Y3d_{3/2}$ and $Y3d_{5/2}$ lines corresponding to the Y-O bonding in the Y_2O_3 lattice are observed at 158.0 and 156.6 eV,[97] Figure 3C. As shown in Figure 3D, the $Yb4d_{3/2}$, $Yb4d_{5/2}$, $Er4d_{3/2}$ and $Er4d_{5/2}$ lines attributed to the host lattice are also detected between 170 and 200 eV.[99,100] The binding energy peaks of Er5s, Li1s and Yb5s overlap within the rage of 50 to 70 eV, making it extremely difficult to detect the Li1s energy band at low Li^+ contents. However, increasing Li^+ amount to *x*=0.070 and 0.123, a larger photoemission signal of Li1s at 55.9 eV was detected,[101] proving the presence of Li^+ on the surface of the nanoparticles (Figure 3E). In conclusion, XPS results reveal the number of carbon groups and the amount of Li^+ on the surface of the nanoparticles increase with increasing the Li content. No significant change in the number of OH groups is observed, though.

To quantify the effect of Li^+ doping on the upconversion emission quantum yield of the nanoparticles, *x*=0.000, 0.008, 0.018, 0.031, 0.070 and 0.123, radiant flux measurements were carried out (Table S2 in ESI). As shown in Figure 4A, the spectral flux intensities of Er^{3+} upconversion emission are higher for Li^+ bearing samples.

Upconversion emission quantum yield q is given by:[16]

$$q = \frac{\int_{\lambda_{min}}^{\lambda_{max}} [S(\lambda)\lambda] d\lambda}{P\lambda} \quad (1)$$

where S(λ) is the spectral radiant flux in W nm^{-1}, λ is the wavelength, and P is the laser power. The corresponding error, Δq, is estimated from the combination of statistical and experimental errors given by:

$$(\Delta q)^2 = \left(\frac{\partial q}{\partial P}\Delta P\right)^2 + \left(\frac{\partial q}{\partial \lambda}\Delta\lambda\right)^2 + \left(\frac{\partial q}{\partial S}\Delta S\right)^2 \quad (2)$$

$$= \frac{1}{(P\lambda)^2}\left(\left(-\int [S(\lambda)\lambda] d\lambda \frac{\Delta P}{\mathrm{P}}\right)^2 + \left(\left(S(\lambda)\lambda^2 - \int [S(\lambda)\lambda] d\lambda\right)\frac{\Delta\lambda}{\lambda}\right)^2 + \left(\left(\int \lambda d\lambda\right)\Delta S\right)^2\right)$$

where $\Delta P/P$=0.05, $\Delta\lambda$=0.10 nm (emission spectra resolution) and $\Delta S/S$=0.10 (according to the manufacturer).

The quantum yields increase linearly reaching maximum values of 0.004, 0.007, 0.034, 0.040, 0.028 and 0.019% at 238 W cm^{-2}, for nanoparticles with *x*=0.000, 0.008, 0.018, 0.031, 0.070 and 0.123, respectively. The maximum value of the emission quantum yield determines the onset of the saturation regime, as reported for $NaYF_4$:Yb^{3+}/Er^{3+} [18] and SrF_2:Yb^{3+}/Er^{3+} nanoparticles,[13] as well as for $NaYF_4$:Yb^{3+}/Er^{3+}[20,102] and La_2S_3:Yb^{3+}/Er^{3+} bulk phosphors.[103] A decrease of the quantum yield at higher laser power density (Figure 4B) is ascribed to the saturation of excited states, in accord with previous reports.[17,104,105]

The maximum quantum yield of 0.0040% for Li^+ free (*x*=0.000) nanoparticles (size 20.3±0.6 nm) is comparable with the maximum quantum yield of 0.0057% at 390 W cm^{-2}, reported for SrF_2:20%Yb^{3+}/2%Er^{3+} nanoparticles (average size 40 nm).[16,18] At a given laser power density, the quantum yield increases significantly for samples containing Li^+, with *x*=0.031 (the optimal concentration) exhibiting a tenfold increase. Furthermore, the quantum yield depends on the lattice parameter and crystallite size, Figure 5. Clearly, quantum yield enhancement correlates with both, the decrease of the unit cell parameter of the host lattice, leading to the modification of the local crystal field symmetry of emitting Er^{3+}, and to crystallite size expansion. Our quantitative results are in accord with previous suggestions that upcoversion enhancement depends on unit cell parameter and crystal size (Table S1 in ESI).[34–37,42,46,50,69,72] However, it is not straightforward to compare the Li^+-based upconversion enhancement results reported in the literature, as no quantitative luminescence measurements are available, Table S1 in ESI.

Conclusions

The preparation of Li^+-doped nanoparticles of $(Y_{0.97-x}Yb_{0.02}Er_{0.01}Li_x)_2O_3$, x=0.000–0.123, by co-precipitation and solid-state reaction was studied. Elemental analysis revealed the former method is unsuitable for achieving such doping. The effect of Li^+ doping on the particle size, lattice parameters, and upconversion emission quantum yield was investigated. Particle size (from 20 to 81 nm) and quantum yield (from 0.004 to 0.040%) increased with increasing Li^+ doping up to x=0.123. Rietveld refinement showed the unit cell parameter decreases upon Li^+ incorporation, indicating the modification of the local Er^{3+} crystal field symmetry. XPS and thermogravimetry indicated the number of OH^- groups does not change significantly with increasing Li^+ content. In contrast, XPS and FTIR revealed the number of carbonate groups on the nanoparticle's surface increased with increasing Li^+ content, ruling out the role of such species as upconversion emission quenchers. In contrast with previous studies, whose nature is essentially qualitative, our quantitative results show particle size increment and lattice parameter decrease are the prime sources of upconversion enhancement. Although $(YYbEr)_2O_3$ is used here as a model system, it is of interest to explore the possibility that these conclusions also hold for other Li^+-doped lanthanide oxide upconverting host nanoparticles. Indeed, Li^+-induced enhancement has been observed for different oxide host lattices, including Y_2O_3, Gd_2O_3, and ZnO, as well as for different lanthanide dopants, Er, Yb/Tm, Yb/Ho, and Yb/Er.[39] Work is in progress to demonstrate how generic our conclusions are and to get insight into the reasons why the above-mentioned parameters are the most important contributions to upconversion enhancement in Li^+-doped nanoparticles and to disentangle the respective roles in the enhancement.

Conflicts of interest

There are no conflicts to declare.

Acknowledgements

This work was partially developed in the scope of the project CICECO-Aveiro Institute of Materials (Ref. No. FCT UID /CTM /50011/2013), financed by national funds through the FCT/MEC and when applicable co-financed by FEDER under the PT2020 Partnership Agreement. Financial support of Fundação para a Ciência e a Tecnologia (FCT) under projects PTDC/CTMNAN/4647/2014, POCI-01-0145-FEDER-016687 and POCI-01-0145-FEDER-031469 is acknowledged. MLD and JCR thank, respectively, FCT for the post-doctoral grant (SFRH/BPD/93884/2013) and FAME Master Program for the Erasmus Mundus scholarship.

References

1 B. Zhou, B. Shi, D. Jin and X. Liu, *Nat. Nanotechnol.*, 2015, **10**, 924–936.

2 X. Y. Huang, S. Y. Han, W. Huang and X. G. Liu, *Chem. Soc. Rev.*, 2013, **42**, 173–201.

3 G. Y. Chen, H. L. Qju, P. N. Prasad and X. Y. Chen, *Chem. Rev.*, 2014, **114**, 5161–5214.

4 J. C. Goldschmidt and S. Fischer, *Adv. Opt. Mater.*, 2015, **3**, 510–535.

5 J.-C. Boyer, F. Vetrone, L. A. Cuccia and J. A. Capobianco, *J. Am. Chem. Soc.*, 2006, **128**, 7444–7445.

6 F. Wang, Y. Han, C. S. Lim, Y. Lu, J. Wang, J. Xu, H. Chen, C. Zhang, M. Hong and X. Liu, *Nature*, 2010, **463**, 1061–1065.

7 M. Bettinelli, L. Carlos and X. Liu, *Phys. Today*, 2015, **68**, 38–44.

8 M. L. Debasu, D. Ananias, I. Pastoriza-Santos, L. M. Liz-Marzán, J. Rocha and L. D. Carlos, *Adv. Mater.*, 2013, **25**, 4868–4874.

9 M. Hu, D. D. Ma, Y. Z. Cheng, C. C. Liu, Z. P. Zhang, Y. J. Cai, S. Wu and R. F. Wang, *J. Mater. Chem. B*, 2017, **5**, 2662–2670.

10 J. Zhao, D. Jin, E. P. Schartner, Y. Lu, Y. Liu, A. V Zvyagin, L. Zhang, J. M. Dawes, P. Xi, J. A. Piper, E. M. Goldys and T. M. Monro, *Nat. Nanotechnol.*, 2013, **8**, 729.

11 S. Fischer, R. Martín-Rodríguez, B. Fröhlich, K. W. Krämer, A. Meijerink and J. C. Goldschmidt, *J. Lumin.*, 2014, **153**, 281–287.

12 S. Wilhelm, *ACS Nano*, 2017, **11**, 10644–10653.

13 M. D. Wisser, S. Fischer, P. C. Maurer, N. D. Bronstein, S. Chu, A. P. Alivisatos, A. Salleo and J. A. Dionne, *ACS Photonics*, 2016, **3**, 1523–1530.

14 U. Resch-Genger and H. H. Gorris, *Anal. Bioanal. Chem.*, 2017, **409**, 5855–5874.

15 G. Gao, D. Busko, S. Kauffmann-Weiss, A. Turshatov, I. A. Howard and B. S. Richards, *J. Mater. Chem. C*, 2017.

16 S. Balabhadra, M. L. Debasu, C. D. S. Brites, R. A. S. Ferreira and L. D. Carlos, *J. Lumin.*, 2017, **189**, 64–70.

17 M. Kaiser, C. Wurth, M. Kraft, I. Hyppanen, T. Soukka and U. Resch-Genger, *Nanoscale*, 2017, **9**, 10051–10058.

18 J. C. Boyer and F. van Veggel, *Nanoscale*, 2010, **2**, 1417–1419.

19 A. Pilch, B. Czaban, D. Wawrzyńczyk and A. Bednarkiewicz, *J. Lumin.*, 2018, DOI: 10.1016/j.jlumin.2018.02.070.

20 D. O. Faulkner, S. Petrov, D. D. Perovic, N. P. Kherani and G. A. Ozin, *J. Mater. Chem.*, 2012, **22**, 24330–24334.

21 S. Kuznetsov, Y. Ermakova, V. Voronov, P. Fedorov, D. Busko, I. A. Howard, B. S. Richards and A. Turshatov, *J. Mater. Chem. C*, 2018, **6**, 598–604.

22 D. Lisjak, O. Plohl, M. Ponikvar-Svet and B. Majaron, *RSC Adv.*, 2015, **5**, 27393–27397.

23 S. Lahtinen, A. Lyytikäinen, H. Päkkilä, E. Hömppi, N. Perälä, M. Lastusaari and T. Soukka, *J. Phys. Chem. C*, 2017, **121**, 656–665.

24 F. Vetrone, R. Naccache, V. Mahalingam, C. G. Morgan and J. A. Capobianco, *Adv. Funct. Mater.*, 2009, **19**, 2924–2929.

25 S. Y. Han, R. R. Deng, X. J. Xie and X. G. Liu, *Angew. Chem. Int. Ed.*, 2014, **53**, 11702–11715.

26 C. Chen, C. Li and Z. Shi, *Adv. Sci.*, 2016, **3**, 1600029.

27 J. Zhou, S. Wen, J. Liao, C. Clarke, S. A. Tawfik, W. Ren, C. Mi, F. Wang and D. Jin, *Nat. Photonics*, 2018, **12**, 154–158.

28 W. Xu, X. Chen and H. Song, *Nano Today*, 2017, **17**, 54–78.

29 Q. Q. Dou and Y. Zhang, *Langmuir*, 2011, **27**, 13236–13241.

30 A. P. Jadhav, J. H. Oh, S. W. Park, H. Choi, B. K. Moon, B. C.

Choi, K. Jang, J. H. Jeong, S. S. Yi and J. H. Kim, *Curr. Appl. Phys.*, 2016, **16**, 1374–1381.
31 D. G. Li, W. P. Qin, P. Zhang, L. L. Wang, M. Lan and P. B. Shi, *Opt. Mater. Express*, 2017, **7**, 329–340.
32 Y. B. Wang, T. Wei, X. W. Cheng, H. Ma, Y. Pan, J. Xie, H. Q. Su, X. J. Xie, L. Huang and W. Huang, *J. Mater. Chem. C*, 2017, **5**, 3503–3508.
33 C. Mao, X. Yang and L. Zhao, *Chem. Eng. J.*, 2013, **229**, 429–435.
34 Q. Cheng, J. H. Sui and W. Cai, *Nanoscale*, 2012, **4**, 779–784.
35 B. S. Cao, Y. Y. He, Z. Q. Feng, M. Song and B. Dong, *Opt. Commun.*, 2011, **284**, 3311–3314.
36 T. Fan and J. Lu, *Opt. Commun.*, 2013, **300**, 5–7.
37 Y. Bai, K. Yang, Y. Wang, X. Zhang and Y. Song, *Opt. Commun.*, 2008, **281**, 2930–2932.
38 X. X. Luo and W. H. Cao, *J. Mater. Res.*, 2008, **23**, 2078–2083.
39 G. Chen and L. Xu, *Am. J. Eng. Appl. Sci.*, 2016, **9**, 79–83.
40 D. H. Kim, J. H. Ryu, J. H. Chung, K. B. Shim and S. Y. Cho, *J. Electrochem. Soc.*, 2011, **158**, J345–J348.
41 W. Y. He, X. F. Wang, J. Zheng and X. H. Yan, *Mater. Res. Innov.*, 2014, **18**, 376–379.
42 K. Mishra, S. K. Singh, A. K. Singh and S. B. Rai, *Mater. Res. Bull.*, 2013, **48**, 4307–4313.
43 P. Singh, P. K. Shahi, A. Rai, A. Bahadur and S. B. Rai, *Opt. Mater. (Amst).*, 2016, **58**, 432–438.
44 D. Avram, B. Cojocaru, I. Tiseanu, M. Florea and C. Tiseanu, *J. Phys. Chem. C*, 2017, **121**, 14274–14284.
45 Z. S. Chen, T. F. Chen, W. P. Gong, W. Y. Xu, D. Y. Wang and Q. K. Wang, *J. Am. Ceram. Soc.*, 2013, **96**, 1857–1862.
46 L. Li, X. T. Wei, X. Q. Cao, K. M. Deng, Q. H. Chen, Y. H. Chen, C. X. Guo and M. Yin, *J. Nanosci. Nanotechnol.*, 2011, **11**, 9892–9898.
47 M. Misiak, B. Cichy, A. Bednarkiewicz and W. Strek, *J. Lumin.*, 2014, **145**, 956–962.
48 H. H. T. Vu, T. S. Atabaev, N. D. Nguyen, Y. H. Hwang and H. K. Kim, *J. Sol-Gel Sci. Technol.*, 2014, **71**, 391–395.
49 R. V Yadav, S. K. Singh and S. B. Rai, *Rsc Adv.*, 2015, **5**, 26321–26327.
50 T. V Gavrilovic, D. J. Jovanovic, L. V Trandafilovic and M. D. Dramicanin, *Opt. Mater. (Amst).*, 2015, **45**, 76–81.
51 I. N. Stanton, J. A. Ayres and M. J. Therien, *Dalt. Trans.*, 2012, **41**, 11576–11578.
52 A. Pandey, V. K. Rai and K. Kumar, *Spectrochim. Acta Part a-Molecular Biomol. Spectrosc.*, 2014, **118**, 619–623.
53 D. Y. Li, Y. X. Wang, X. R. Zhang, H. X. Dong, L. Liu, G. Shi and Y. L. Song, *J. Appl. Phys.*, 2012, **112**, 094701.
54 L. Liu, Y. X. Wang, X. R. Zhang, K. Yang, Y. F. Bai, C. H. Huang and Y. L. Song, *Opt. Commun.*, 2011, **284**, 1876–1879.
55 A. Dubey, A. K. Soni, A. Kumari, R. Dey and V. K. Rai, *J. Alloys Compd.*, 2017, **693**, 194–200.
56 Q. Sun, X. Q. Chen, Z. K. Liu, F. P. Wang, Z. H. Jiang and C. Wang, *J. Alloys Compd.*, 2011, **509**, 5336–5340.
57 Q. Sun, H. Zhao, X. Q. Chen, F. P. Wang, W. Cai and Z. H. Jiang, *Mater. Chem. Phys.*, 2010, **123**, 806–810.
58 M. Z. Yang, Y. Sui, H. W. Mu, S. C. Lu, X. J. Wang and T. Q. Lu, *J. Rare Earths*, 2011, **29**, 1022–1025.
59 Y. F. Bai, Y. X. Wang, G. Y. Peng, K. Yang, X. R. Zhang and Y. L. Song, *J. Alloys Compd.*, 2009, **478**, 676–678.
60 Y. F. Bai, Y. X. Wang, G. Y. Peng, W. Zhang, Y. K. Wang, K. Yang, X. R. Zhang and Y. L. Song, *Opt. Commun.*, 2009, **282**, 1922–1924.
61 H. J. Liang, Y. D. Zheng, G. Y. Chen, L. Wu, Z. G. Zhang and W. W. Cao, *J. Alloys Compd.*, 2011, **509**, 409–413.
62 Y. T. Jia, Y. L. Song, Y. F. Bai and Y. X. Wang, *Luminescence*, 2011, **26**, 259–263.
63 Y. L. Ding, X. D. Zhang, H. B. Gao, S. Z. Xu, C. C. Wei and Y. Zhao, *J. Alloys Compd.*, 2014, **599**, 60–64.
64 X. Q. Chen, Z. K. Liu, Q. Sun, M. Ye and F. P. Wang, *Opt. Commun.*, 2011, **284**, 2046–2049.
65 Y. Y. Guo, D. Y. Wang and F. Wang, *Opt. Mater. (Amst).*, 2015, **42**, 390–393.
66 M. Z. Yang, Y. Sui, S. P. Wang, X. J. Wang, Y. Q. Sheng, Z. G. Zhang, T. Q. Lu and W. F. Liu, *Chem. Phys. Lett.*, 2010, **492**, 40–43.
67 G. Y. Chen, H. C. Liu, H. J. Liang, G. Somesfalean and Z. G. Zhang, *Solid State Commun.*, 2008, **148**, 96–100.
68 H. J. Liang, G. Y. Chen, H. C. Liu and Z. G. Zhang, *J. Lumin.*, 2009, **129**, 197–202.
69 G. Y. Chen, H. C. Liu, H. J. Liang, G. Somesfalean and Z. G. Zhang, *J. Phys. Chem. C*, 2008, **112**, 12030–12036.
70 V. Mahalingam, R. Naccache, F. Vetrone and J. A. Capobianco, *Opt. Express*, 2012, **20**, 111–119.
71 A. N. Meza-Rocha, E. F. Huerta, U. Caldiño, S. Carmona-Téllez, M. Bettinelli, A. Speghini, S. Pelli, G. C. Righini and C. Falcony, *J. Lumin.*, 2015, **167**, 352–359.
72 G. Y. Chen, H. C. Liu, G. Somesfalean, Y. Q. Sheng, H. J. Liang, Z. G. Zhang, Q. Sun and F. P. Wang, *Appl. Phys. Lett.*, 2008, **92**, 113114.
73 T. Fan, Q. Y. Zhang and Z. H. Jiang, *J. Opt.*, 2011, **13**.
74 H. Niioka, J. Yamasaki, D. T. K. Dung and J. Miyake, *Chem. Lett.*, 2016, **45**, 1406–1408.
75 F. Vetrone, J. C. Boyer, J. A. Capobianco, A. Speghini and M. Bettinelli, *J. Appl. Phys.*, 2004, **96**, 661–667.
76 E. F. Huerta, S. Carmona-Tellez, S. Gallardo-Hernandez, J. G. Cabanas-Moreno and C. Falcony, *Ecs J. Solid State Sci. Technol.*, 2016, **5**, R129–R135.
77 L. D. Sun, C. Qian, C. S. Liao, X. L. Wang and C. H. Yan, *Solid State Commun.*, 2001, **119**, 393–396.
78 A. K. Singh, S. K. Singh and S. B. Rai, *Rsc Adv.*, 2014, **4**, 27039–27061.
79 J.-C. Park, H.-K. Moon, D.-K. Kim, S.-H. Byeon, B.-C. Kim and K.-S. Suh, *Appl. Phys. Lett.*, 2000, **77**, 2162–2164.
80 E. L. Cates, A. P. Wilkinson and J. H. Kim, *J. Phys. Chem. C*, 2012, **116**, 12772–12778.
81 S. L. Gai, P. P. Yang, D. Wang, C. X. Li, N. Niu, F. He and X. B. Li, *Crystengcomm*, 2011, **13**, 5480–5487.
82 Z. S. Chen, W. P. Gong, T. F. Chen and S. L. Li, *Bull. Mater. Sci.*, 2011, **34**, 429–434.
83 K. J. Boyd, D. Marton, S. S. Todorov, A. H. Albayati, J. Kulik, R. A. Zuhr and J. W. Rabalais, *J. Vac. Sci. Technol. a-Vacuum Surfaces Film.*, 1995, **13**, 2110–2122.
84 C. D. S. Brites, X. Xie, M. L. Debasu, X. Qin, R. Chen, W. Huang, J. Rocha, X. Liu and L. D. Carlos, *Nat. Nanotechnol.*, 2016, **11**, 851–856.

85 T. V Gavrilovic, D. J. Jovanovic, V. M. Lojpur, V. Dordevic and M. D. Dramicanin, *J. Solid State Chem.*, 2014, **217**, 92–98.

86 L. N. Guo, Y. H. Wang, Y. Z. Wang, J. Zhang, P. Y. Dong and W. Zeng, *Nanoscale*, 2013, **5**, 2491–2504.

87 J. Chen, C. H. Li, Z. Hui and Y. G. Liu, *Inorg. Chem.*, 2017, **56**, 1144–1151.

88 M. Y. Peng, X. W. Yin, P. A. Tanner, C. Q. Liang, P. F. Li, Q. Y. Zhang and J. R. Qiu, *J. Am. Ceram. Soc.*, 2013, **96**, 2870–2876.

89 C. C. Lin and R. S. Liu, *J. Phys. Chem. Lett.*, 2011, **2**, 1268–1277.

90 E. Foran, S. Weiner and M. Fine, *Sci. Rep.*, 2013, **3**, 1700.

91 T. Andelman, S. Gordonov, G. Busto, P. V Moghe and R. E. Riman, *Nanoscale Res. Lett.*, 2010, **5**, 263–273.

92 A. P. Dementjev, A. de Graaf, M. C. M. van de Sanden, K. I. Maslakov, A. V Naumkin and A. A. Serov, *Diam. Relat. Mater.*, 2000, **9**, 1904–1907.

93 T. L. Barr and S. Seal, *J. Vac. Sci. Technol. a-Vacuum Surfaces Film.*, 1995, **13**, 1239–1246.

94 S. Bhattacharyya, J. Hong and G. Turban, *J. Appl. Phys.*, 1998, **83**, 3917–3919.

95 D. Majumdar and D. Chatterjee, *J. Appl. Phys.*, 1991, **70**, 988–992.

96 R. P. Vasquez, M. C. Foote and B. D. Hunt, *J. Appl. Phys.*, 1989, **66**, 4866–4877.

97 S. A. Barve, Jagannath, N. Mithal, M. N. Deo, N. Chand, B. M. Bhanage, L. M. Gantayet and D. S. Patil, *Surf. Coatings Technol.*, 2010, **204**, 3167–3172.

98 P. Parnicka, P. Mazierski, T. Grzyb, Z. Wei, E. Kowalska, B. Ohtani, W. Lisowski, T. Klimczuk and J. Nadolna, *J. Catal.*, 2017, **353**, 211–222.

99 Y. Ohno, *J. Electron Spectros. Relat. Phenomena*, 2008, **165**, 1–4.

100 F.-H. Chen, J.-L. Her, Y.-H. Shao, Y. H. Matsuda and T.-M. Pan, *Nanoscale Res. Lett.*, 2013, **8**, 1–5.

101 M.-L. Shek, J. Hrbek, T. K. Sham and G.-Q. Xu, *Phys. Rev. B*, 1990, **41**, 3447–3454.

102 R. H. Page, K. I. Schaffers, P. A. Waide, J. B. Tassano, S. A. Payne, W. F. Krupke and W. K. Bischel, *J. Opt. Soc. Am. B-Optical Phys.*, 1998, **15**, 996–1008.

103 Y. M. Yang, C. Mi, F. Y. Jiao, X. Y. Su, X. D. Li, L. L. Liu, J. Zhang, F. Yu, Y. Z. Liu and Y. H. Mai, *J. Am. Ceram. Soc.*, 2014, **97**, 1769–1775.

104 M. Pollnau, D. R. Gamelin, S. R. Luthi, H. U. Gudel and M. P. Hehlen, *Phys. Rev. B*, 2000, **61**, 3337–3346.

105 J. F. Suyver, A. Aebischer, S. Garcia-Revilla, P. Gerner and H. U. Gudel, *Phys. Rev. B*, 2005, **71**, 125123.

Li^+-doped $(Y_{0.97-x}Yb_{0.02}Er_{0.01}Li_x)_2O_3$ nanoparticles, x=0.000–0.123, are prepared by solid-state reaction; Li^+-induced upconversion enhancement is quantitatively assessed.

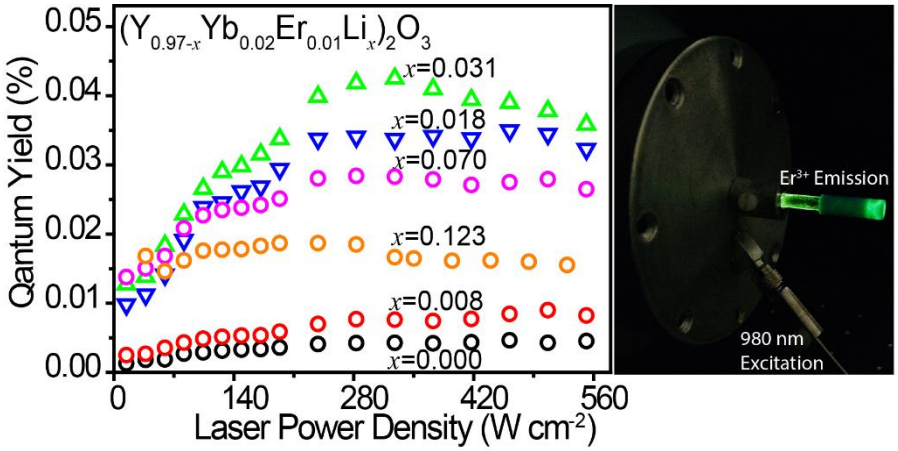

Figures and Tables

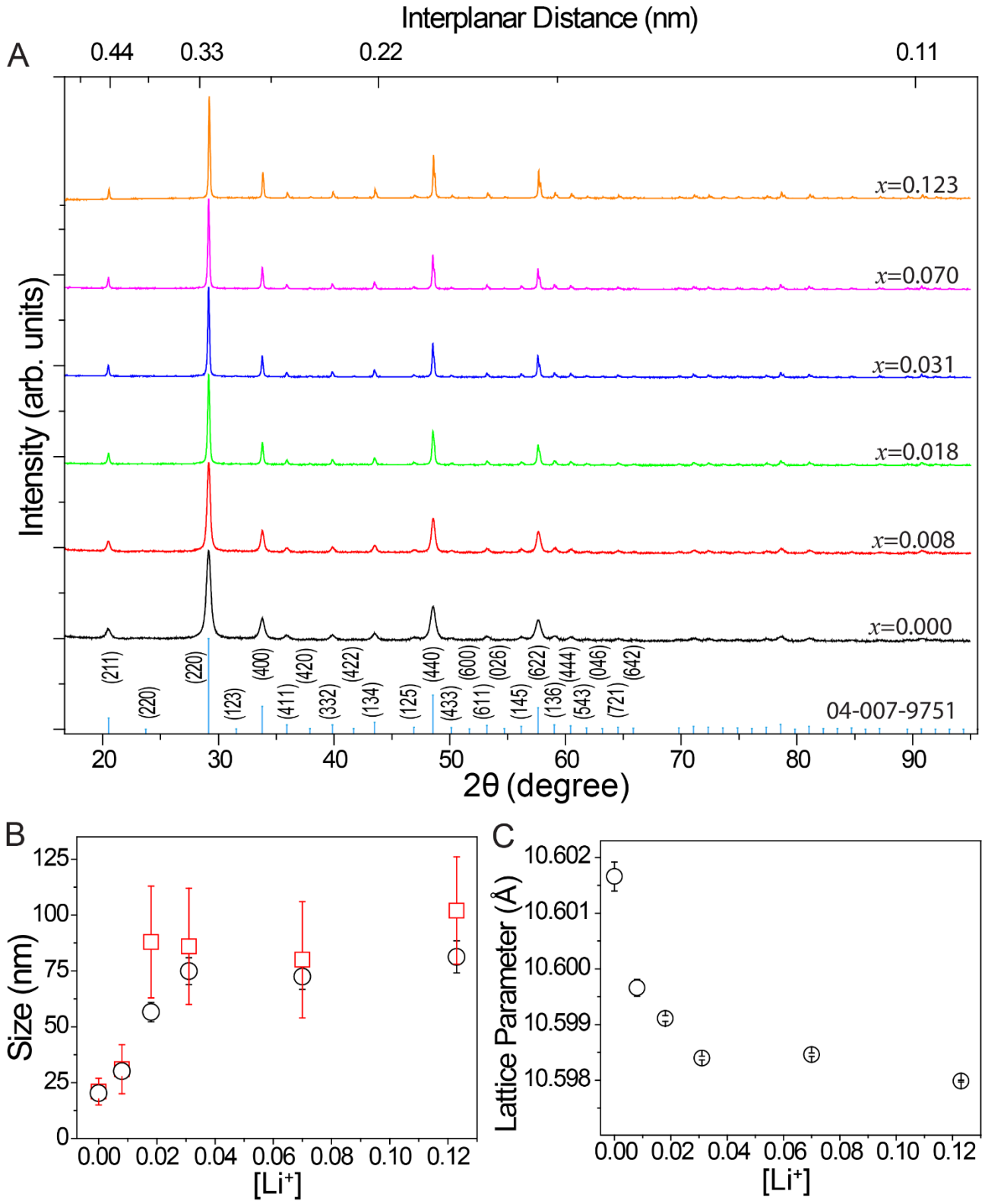

Figure 1. A) Powder XRD patterns of the nanoparticles and reference cubic Y_2O_3 (04-007-9751). B) Evolution of the XRD (circles) and TEM (squares) particle size with Li^+ doping. C) Lattice parameter dependence on the Li^+ content.

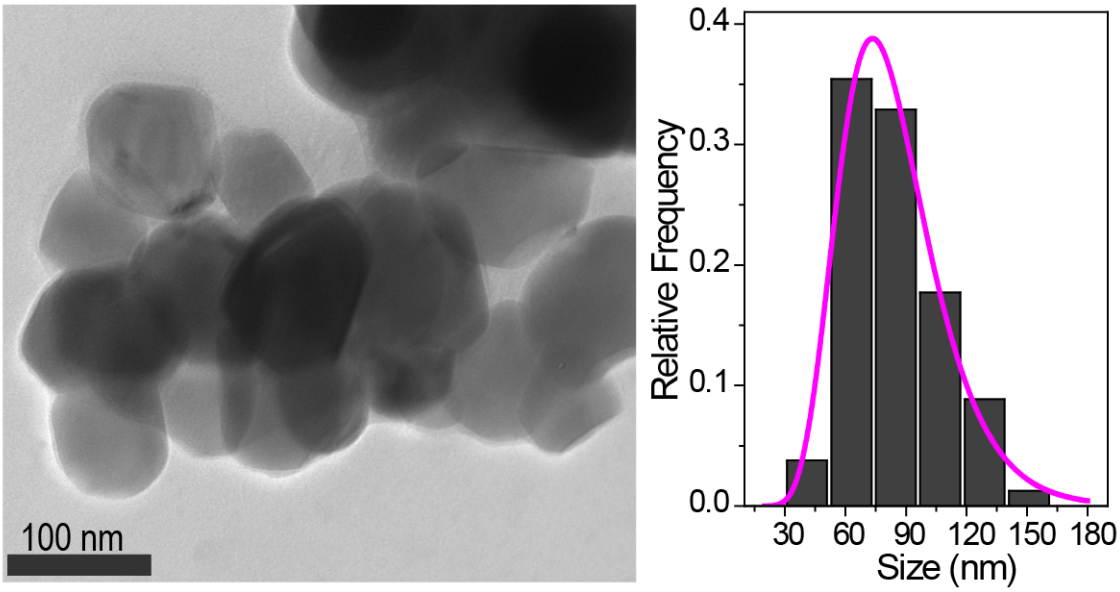

Figure 2. A representative STEM image of the nanoparticles with *x*=0.070. The corresponding particle size distribution histogram is shown on the right (solid line of the histogram is the best fit using a log-normal distribution with average size 80±26, r^2>0.98).

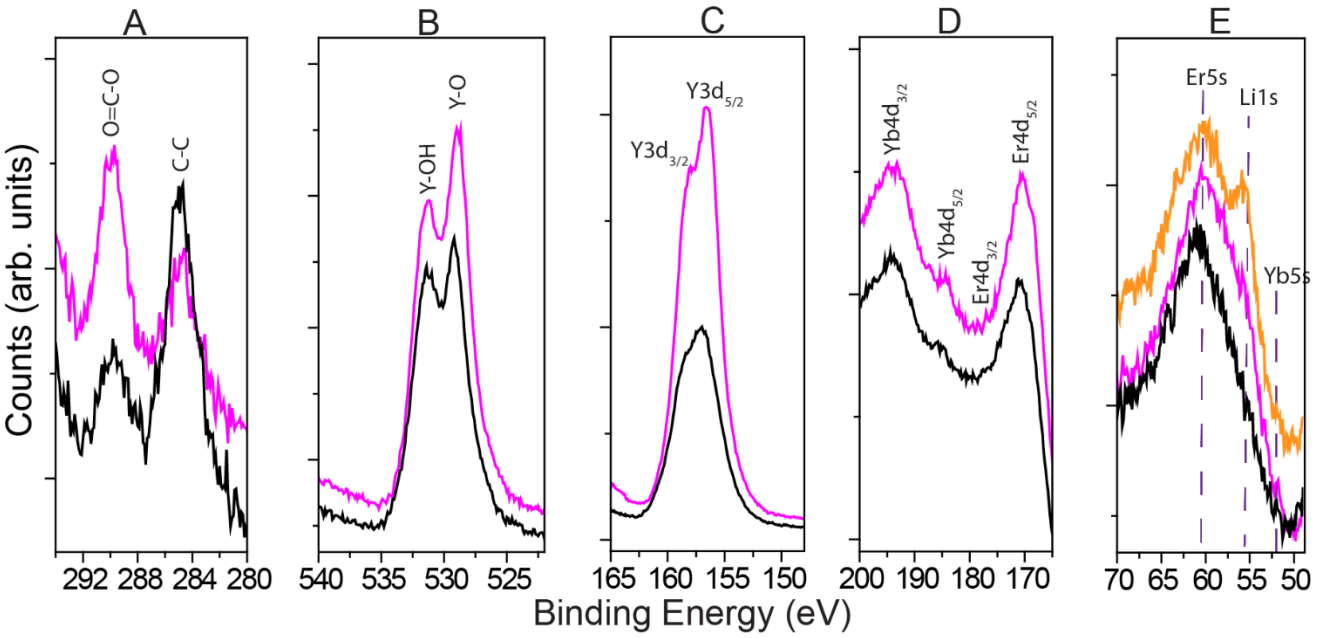

Figure 3. XPS spectra of A) C1s, B) O1s, C) Y3d, D) Yb4d/Er4d, and E) Er5s/Li1s/Yb5s binding energy lines for the nanoparticles: *x*=0.000 (black lines) and *x*=0.070 (magenta lines). The orange line in E) is for *x*=0.123 with the highest Li^+ content (Table 2), clearly showing the signal of the Li1s binding energy; vertical dashed lines denote the peak positions of the Er5s, Li1s and Yb5s lines.

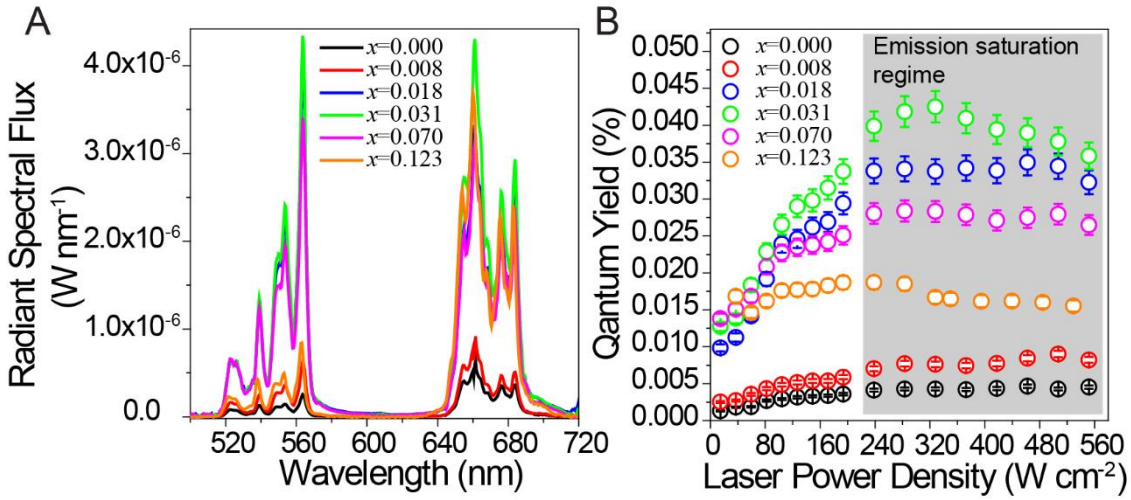

Figure 4. A) Emission spectral flux of nanoparticles excited with a 980-nm diode laser, at a power density of 179 Wcm^{-2}. B) Evolution of the corresponding quantum yields (calculated using Equation 1) with the laser power density.

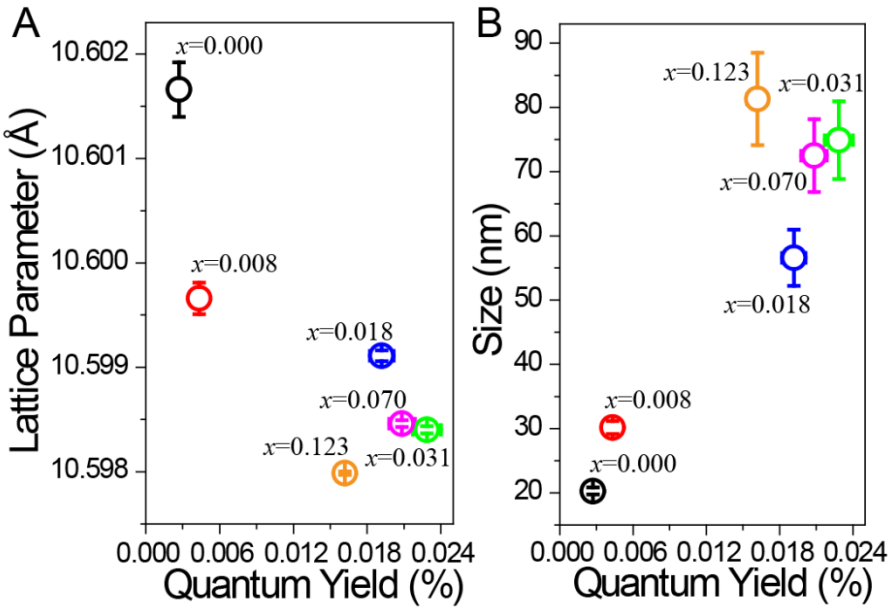

Figure 5. A) Dependence of the quantum yield on the lattice parameter, and B) on the nanoparticle size. Laser power density 81 W cm^{-2}.

Table 1. ICP-AES elemental analysis of Li^+ doped nanoparticles, $(Y_{0.97-n}Yb_{0.02}Er_{0.01}Li_n)_2O_3$, with nominal n=0.05 and 0.15 prepared by the co-precipitation method.

Mole Fraction	Y	Er	Yb	Li
Nominal	0.920	0.010	0.020	0.050
Measured	0.962	0.012	0.025	0.000
Nominal	0.820	0.010	0.020	0.150
Measured	0.964	0.012	0.023	0.000

Table 2. ICP-AES elemental analysis of $(Y0.9_{7-x}Yb_{0.02}Er0_{.01}Li_x)_2O_3$ nanoparticles (x represents measured molar content) prepared by solid-state reaction.

Mole Fraction	Y	Er	Yb	Li	Sample Ref. *x*
Nominal	0.970	0.010	0.020	0.000	---
Measured	0.964	0.012	0.024	0.000	0.000
Nominal	0.960	0.010	0.020	0.010	---
Measured	0.958	0.011	0.024	0.008	0.008
Nominal	0.945	0.010	0.020	0.025	---
Measured	0.948	0.011	0.022	0.018	0.018
Nominal	0.920	0.010	0.020	0.050	---
Measured	0.932	0.012	0.025	0.031	0.031
Nominal	0.870	0.010	0.020	0.100	---
Measured	0.894	0.012	0.024	0.070	0.070
Nominal	0.820	0.010	0.020	0.150	---
Measured	0.823	0.018	0.036	0.123	0.123